npj | 2D Materials and Applications

www.nature.com/npj2dmaterials

ARTICLE OPEN

Inkjet-printed CMOS-integrated graphene–metal oxide sensors for breath analysis

Tien-Chun Wu[1], Andrea De Luca[2], Qinyu Zhong[1], Xiaoxi Zhu[1], Osarenkhoe Ogbeide[1], Doo-Seung Um[1], Guohua Hu[1], Tom Albrow-Owen[1], Florin Udrea[2] and Tawfique Hasan[1*]

Early diagnosis in exhaled breath is a key technology for next-generation personal healthcare monitoring. Current chemiresistive sensors, primarily based on metal oxide (MOx) thin films, have limited applicability in such portable systems due to their high power consumption, long recovery time, poor device-to-device consistency, and baseline drifts. To address these challenges for ammonia (NH_3) detection in exhaled breath, a critical biomarker for a variety of kidney and liver problems, we present a formulation of a graphene–MOx functional ink-based sensing platform. We integrate our sensing layer directly onto miniaturized CMOS microhotplates (μHP) via inkjet printing, potentially enabling scalability and device-to-device performance repeatability. Using stage-by-stage temporal analysis, and a temperature-pulsed modulation (TM) strategy, we achieve ultrahigh responsivity (1500% at 10 ppm pure NH_3), fast response and recovery time (28 and 43 s), ultralow power consumption (~6 mW), negligible baseline drift (<0.67%), excellent cross-device and cross-cycle consistency (<0.5% and <0.41% variation in responsivity) and long-term stability (<1% variation) in our graphene–zinc oxide (ZnO) formulation, outperforming conventional MOx chemiresistive sensors. We further mitigate the effect of humidity through our measurement protocols, while interference from acetone is compensated through the parallel deployment of an additional inkjet printed graphene–tungsten oxide (WO_3) device as part of the sensor array. Our dual graphene–MOx formulations and their integration with ultralow power CMOS through inkjet printing represent a significant step towards reliable and portable multi-analyte breath diagnostics.

npj 2D Materials and Applications (2019)3:42 ; https://doi.org/10.1038/s41699-019-0125-3

INTRODUCTION

Increasing awareness of personal health conditions is rapidly promoting the development of point-of-care technologies for early diagnosis of diseases. Breath analysis is an important candidate among the various diagnostic technologies available.[1,2] This is due to its non-invasive approach for detecting unique chemical signatures that can be correlated with specific diseases.[1,2] Among the various species in exhaled breath, ammonia (NH_3) is a critical biomarker associated with a range of kidney and liver disorders.[2,3] The new generation NH_3 diagnostic systems rely on the development of low-cost, miniaturized devices in which semiconducting metal oxides (MOx) are commonly utilized as the sensing layer among chemiresistive sensors.[4] In particular, ZnO has been long exploited for NH_3 detection due to its strong response compared to other MOx materials.[5,6] However, devices with MOx as the active sensing layer often requires continuous operation at elevated temperatures which not only consumes high power but also deteriorates material's structural stability, leading to shortened lifetime and compromised responses.[7] Incorporation of atomically thin graphene into MOx matrix has recently attracted strong interest due to its excellent sensitivity to environmental perturbation[8] and low work function,[9] enabling lower operating temperatures.[10] The graphene–MOx hybrids reported to date exhibit improved responsivity[11] which is attributed to the formation of local metal–semiconducting (M–S) heterojunctions.[12,13] They also show enhancement in gas adsorption capability at the active graphene sites.[12,14] Despite the improved responsivity, critical issues common to chemiresistive sensors, such as high power consumption, long recovery time,[15–17] severe baseline drift,[11,14,17] low signal-to-noise ratio (SNR) and unstable responses,[11,14,17] poor device-to-device consistency,[18] interference with volatile organic compounds (VOCs)[9] and water vapor,[19] remain unresolved. Limited attempts based on dynamic control of operating temperature have been applied to improve detection limit,[20] baseline drift,[21] cross-selectivity,[22,23] and power consumption of MOx and 2D material gas sensors. However, these approaches have not been sufficiently effective to resolve the issues,[21] and lack systematic and quantitative experimental support.[20,21] This has inhibited a satisfactory understanding of the underlying mechanisms and their interplay. The aforementioned challenges all hinder diagnostic applications[2] and cannot be easily addressed through the sensing material alone.[1,2] Instead, a holistic solution is necessary to realize devices suitable for personal healthcare monitoring.

Here, we present a graphene–MOx hybrid-sensing material that is integrated onto a (1 × 1 mm) CMOS microhotplate (μHP). The miniaturized device platform is tailored using inkjet deposition as a high-precision, material-efficient, and scalable technique to produce thin and uniform sensing layers suitable for rapid and consistent detection. We address the shortcomings from previous studies on high power consumption/operating temperatures, long recovery time, and baseline drifts by optimizing the sensing material and ink formulation, together with the development of a temperature modulation strategy and measurement algorithm. In particular, we focus on the studies and control of the complex interplays between surface-analyte molecule adsorption/desorption (both chemically and physically), carrier transport, and analyte diffusion taking place at different temperature conditions, which is realized through efficient and robust operations in the dynamic temperature-programmed modes enabled by the μHP.

[1]Cambridge Graphene Centre, University of Cambridge, Cambridge CB3 0FA, UK. [2]Department of Engineering, University of Cambridge, Cambridge CB3 0FA, UK. *email: th270@cam.ac.uk

Using stage-by-stage temporal analysis, we establish comprehensive quantitative studies on temperature-dependent mechanisms for the material system to develop appropriate algorithms, leading to enhanced sensing performances and reproducibility. Additionally, our approach of using inkjet deposition offers excellent device-to-device consistency, overcoming a common drawback[18] of the majority of the other studies. Cross-selectivity, another weakness of traditional MOx sensors[22] is addressed by an additional graphene–MOx sensor incorporating a second metal oxide. Our dual graphene–MOx inkjet strategy realized on ultralow power CMOS platform, coupled with temperature modulation algorithms represent new opportunities in portable multi-analyte breath diagnostics.

RESULTS

Production and formulation of graphene–metal oxide inks

The overall ink production process involves exfoliation of graphite crystals via ultrasonic-assisted liquid phase exfoliation (UALPE, as detailed in the "Methods" section) into a stable dispersion of few-layer graphene flakes. This dispersion is then mixed with the MOx nanoparticles (NPs) in a solvent mixture to produce the stable, inkjet printable graphene–MOx hybrid functional ink. In UALPE, the selection of suitable solvents and stabilization agents plays a crucial role in preventing the re-stacking of the exfoliated flakes[24] and facilitating stable dispersions.[25] Alcoholic solvents are typically favorable for functional ink formulation due to rapid drying, and excellent substrate wetting due to their low surface tension.[26] However, they are unable to exfoliate and stabilize pristine graphene and other 2D crystals due to large mismatch in Hansen solubility parameters.[25] To address this, dispersants such as polymers have been used to improve the exfoliation and stabilization of graphene flakes in alcohols.[27] We incorporate polyvinylpyrrolidone (PVP) during UALPE, as it can readily adsorb onto graphite surface,[28] and stabilize exfoliated flakes through steric hindrance.[29,30] PVP is also used for the production of stable and homogeneous dispersions of metal oxide NPs.[31,32] In addition, it can act as an ink binder and a rheology modifier[33,34] to improve wetting and jetting properties of the inkjet inks.[35]

However, instead of uniform coverage, ring-like deposition of solutes or suspended particles during drying (known as the *coffee-ring effect*)[36,37] is commonly seen in many mono alcoholic solvent-based inks. To suppress such non-uniform deposition, we employ a binary alcohol mixture-based ink formulation strategy with 90 vol% IPA and 10 vol% 2-butanol composition to our final ink.[38,39] This formulation (surface tension $\gamma_{ink} = 31.12\,mN\,m^{-1}$) allows deformation of the ink droplet and counteracts the capillary flow during drying, while keeping the surface tension low enough for good wetting of the substrate (Si_3N_4 μHP membrane, surface energy $\gamma_{sub} \approx 40\,mN\,m^{-1}$).[40] Indeed, excellent spatial uniformity and consistency across inkjet printed black phosphorus flakes have recently been achieved using a similar strategy.[38]

For ink formulation, we first exfoliate graphene and disperse the MOx NPs separately; see the "Methods" section for details. For graphene–ZnO ink formulation, the effective concentrations (after LPE) of ZnO and graphene in the dispersions are estimated as 26 and $1.2\,mg\,mL^{-1}$, respectively, from thermogravimetric analysis (TGA); Supplementary Fig. S1. The prepared dispersions are sonicated together to obtain a homogeneous and stable ink. By mixing ZnO and graphene dispersions at different ratios, we formulate three graphene–ZnO inks with different graphene loadings (0%: pure ZnO, 3 wt% graphene: ZG-3, 6 wt% graphene: ZG-6) (see Fig. 1a). To determine the optimum loading of graphene in the graphene–ZnO hybrid, these three inks are printed onto the CMOS device for gas characterization. Similar approach is used for the formulation of graphene–WO_3 ink (with $12.5\,mg\,mL^{-1}$) WO_3 which is used to fabricate the accompanying sensor to improve the selectivity.

Characterization of the formulated inks

For inkjet printing, stable ink drop generation is crucial for high-quality printed films. The printability of the ink can be predicted with inverse Ohnesorge number $Z = \sqrt{\gamma_{ink}\rho D}/\eta$,[35,41] where γ_{ink} is surface tension of the ink, η is the viscosity, ρ is the density, and D is the nozzle diameter. As a rule of thumb, studies[35,41] have suggested that stable jetting satisfies Z of 1–14 to avoid the formation of long filament or secondary/satellite droplets. Taking ZG-3 inks as an example, the rheological parameters measured are: $\gamma_{ink} = 31.12\,mN\,m^{-1}$, $\eta = 2.14\,mPa\,s$ at $10^4\,s^{-1}$ (shear-thinning, see Supplementary Fig. S2), $\rho = 0.8\,g\,cm^{-3}$, $D = 21.5\,\mu m$, giving a $Z = 10.8$. This indicates that our inks satisfy optimal jetting requirements for inkjet printing. Supplementary Table S2 summarizes the rheological parameters of the three inks. Complying with the Z estimation, all our inks exhibit similarly stable jetting and droplet formation without the generation of satellite droplets. A typical example of a jetting sequence of our inks is shown in Fig. 1b. The drying dynamics of the ink is also characterized by time-dependent contact angle measurement for the duration of droplet drying onto a clean Si/SiO_2 substrate (Fig. 1c). The initial angle is 18° which indicates a good wetting of the substrate. The contact angle descends as the droplet spreads due to low surface tension, dropping linearly after ≈0.6 s, until the angle saturates at close to 0°. At the same time, after ≈1 s, the diameter of the droplet increases at a reduced speed, suggesting the contribution of Marangoni flow to suppress coffee-ring effect.[37,38] In addition, no sudden perturbation in the contact angle is observed during the drying process. These indicate a good wetting of the substrate and uniformly deposited graphene/ZnO after ink drying.

CMOS μHP device

The architecture of the CMOS μHP platform we use in our work has been reported in prior publications.[42] The miniaturized μHP platform has an ultralow power consumption (down to 1.6 mW),[42] high thermal efficiency (0.11 mW/°C)[21] and fast thermal response (tens of ms),[21] and a highly stable and uniform temperature distribution due to its suspended membrane structure and integrated heat spreading plate. The rapid thermal response enables sensing operation in dynamic temperature-programmed modes.

To fabricate the sensors, we use inkjet printing to deposit the ZnO–graphene functional inks directly onto the interdigitated Au electrodes (IDEs) on the Si_3N_4 membrane substrate (5 μm finger width and gap; 250 μm diameter) of the CMOS μHP. This process enables automated fabrication of multiple devices at once, as schematized in Fig. 1d. Figure 1e shows a typical example of an inkjet-printed graphene–ZnO device (ZG-3). The number of print repetitions (20 passes) is optimized with trade-offs between the uniformity of the printed film, electrical conductivity, and reaction/recovery time of the fabricated sensors. The overview image reveals a printed pattern with high printing definition and uniform material distribution. The zoomed-in image further shows the evenly distributed graphene–ZnO NPs on top of and in-between the IDEs.

Characterization of the printed films

Although PVP improves exfoliation and stabilization of the ink, it is an insulating polymer and is detrimental to the functionality of the graphene–ZnO sensing layer. We therefore remove PVP by decomposing it through annealing at 400 °C[43,44] for 2 h using our μHP in Ar atmosphere. As verified by the TGA data (Supplementary Fig. S3), this condition selectively decomposes PVP to <5 wt% of its

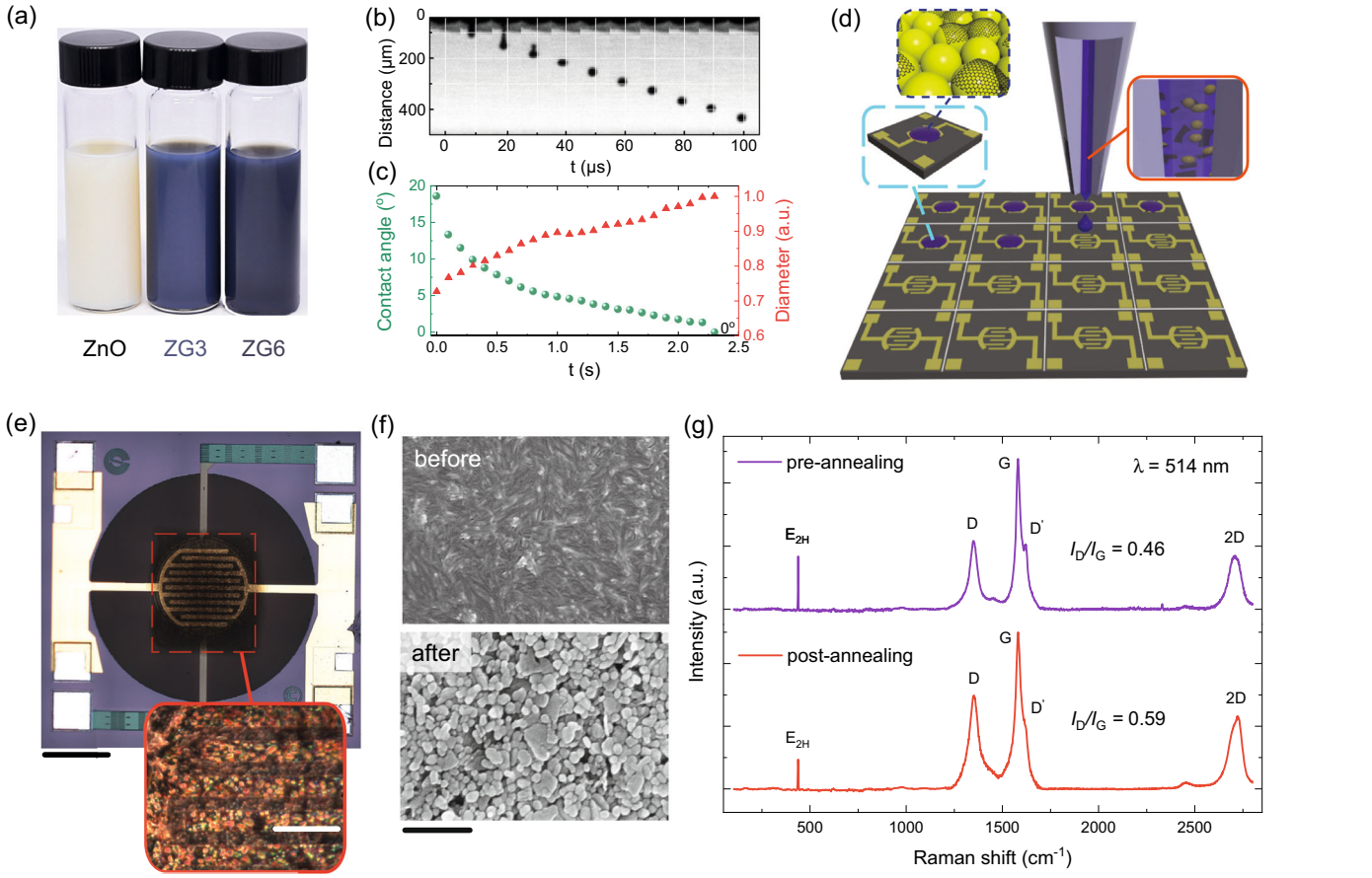

Fig. 1 Characterization of inks and printed thin films. **a** Images of formulated ZnO, ZG-3wt%, ZG-6 wt% inks. **b** Jetting sequence of ZnO/graphene inks, showing rheological properties on the right. **c** Change in contact angle over the drying process. **d** Illustration of the inkjet deposition process. **e** Microscopic image of the inkjet-deposited CMOS sensory device. Scale bar 200 μm. (Inset) Enlarged view: scale bar 20 μm. **f** SEM images of printed ZnO–graphene composite films: pre-annealing on the top, post-annealing on the bottom. Scale bar 250 nm. **g** Raman spectra of ZG-3 printed films pre-annealing and post-annealing treatment, respectively

initial concentration, resulting in a negligible contribution (0.34 wt% of residual) in the annealed film. Figure 1f shows a set of scanning electron microscope (SEM) images comparing pre-annealed and post-annealed inkjet printed ZnO–graphene thin films. The pre-annealed film above shows a matrix of ZnO NPs connected through graphene and PVP polymer; whereas the post-annealed film below shows selective decomposition of PVP. The morphology shows considerable areas of exposure to ZnO NPs. Also, we propose that the porosity of printed film, produced by the decomposition of PVP[45] improves gas diffusion. Although the NPs and LPE flakes could be randomly distributed in sub-micron scale, we argue that the overall uniformity of the sensing material composition across the 250 μm diameter active area remains statistically consistent between multiple devices. The SEM image also shows that the average diameter of the ZnO NPs is ≈40 nm. This correlates well with the average particle size of ≤50 nm specified by the supplier.[46] We therefore believe that the exfoliation process does not alter the particle size but successfully avoids their agglomeration. Supplementary Fig. S4 reveals that the exfoliated graphene flakes have median lateral size and thickness of 150 and 2 nm, respectively.

We also carry out Raman measurements to investigate the composition of the printed inks before and after the annealing step. Figure 1g shows representative Raman spectra (out of 10 similar measurements taken at random locations on the samples). The existence of few layer graphene in the composite film is supported by the shape of the 2D peak which is located at 2720 cm^{-1};[47,48] whereas the signature of ZnO NPs is identified by the E_{2H} peak located at 438 cm^{-1}.[49] The shift in the 2D peak position is likely due to a small increase in edge defects after the annealing step. This also marginally increases the I_D/I_G ratio and merges the D′ with the G peak.[50] Note that PVP does not play an active role in the sensing process, which is distinct from the study presented in ref. [51] where no annealing treatment is made.

Sensing mechanisms under constant operating temperature

Figure 2a illustrates the sensing mechanisms for the detection of pure NH_3 with graphene–ZnO composite studied under constant operating temperature, referred to as the isothermal (ISO) mode, at 300 °C (see Supplementary Fig. S5 for optimization details). The physical representation comprises multiple layers of graphene–ZnO hybrid stacking on each other. We suggest that the porous structure of the printed thin films from LPE graphene[25,45] and the decomposition of PVP[45] establish efficient gas diffusion channels towards the graphene–ZnO heterojunctions at which the bandgap alteration occurs.[12] In an inert gas environment, a relatively small potential barrier is formed at the grain boundaries at the ZnO/ZnO interface;[52] whereas M–S Ohmic contacts are formed at the graphene/ZnO interface.[13,14] We propose that the gas adsorption behavior of graphene–ZnO during NH_3 exposure can be classified as follows. Chemisorption occurring at the ZnO surface leads to increment in the potential barrier between the ZnO NPs. The superior physisorption capability of graphene, especially at the defect sites and ZnO

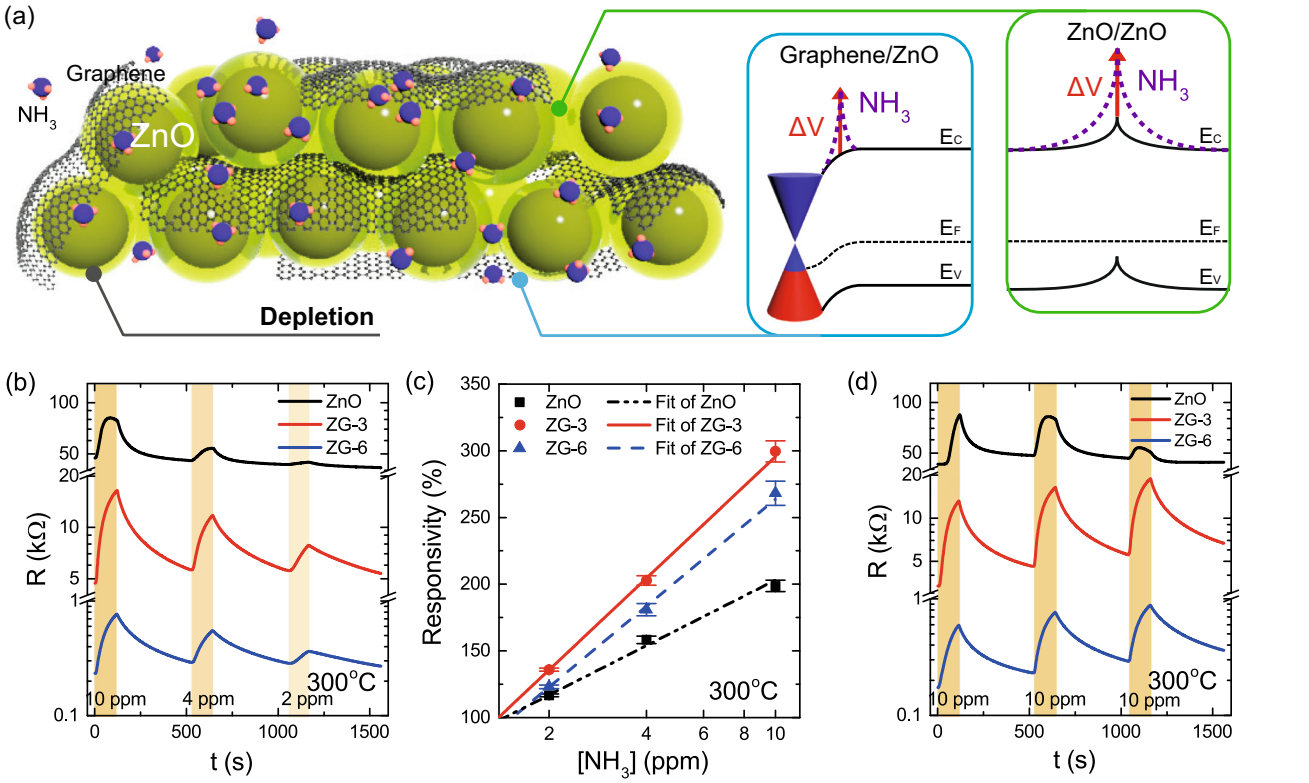

Fig. 2 Response curves for ZnO, ZG-3, ZG-6 in isothermal mode (300 °C). **a** Illustration of sensing mechanism on detection of pure NH_3 with graphene–ZnO composite in ISO mode; band diagrams at the graphene/ZnO and ZnO/ZnO interfaces shown on the right, ΔV arises as NH_3 adsorbs, resulting in enlarged depletion region. **b** Resistance response at 10, 4, 2 ppm of NH_3, respectively. The orange region represents injection of NH_3 in ppm. **c** Responsivity as a function of NH_3 concentration with linear fits. **d** Resistance response at 10 ppm NH_3 repeated over three cycles

interfaces,[12] contributes to the increment in the potential barrier, resulting in an amplification of responsivity compared to that in pure ZnO. The amplification of bandgap alteration at the graphene/ZnO interface due to the higher density of adsorbed gas molecules than at the ZnO surface is the dominating factor for responsivity enhancement.[53] The effective conduction paths consist of a combination of ZnO NPs conduction channels and graphene–ZnO heterojunctions. First, pure ZnO NPs matrix follows neck-controlling model[54] (as $d \geq 2l$, where d is diameter of NP, l is depletion width within individual NPs), where the conductivity is altered by l, and is sensitive to analyte gas concentration (Fig. 2b). Second, increasing the loading of graphene, which provides additional conduction paths between NPs, shows improvement in electron transport as revealed in the lowered resistance value in Fig. 2b. Supplementary Fig. S6 shows a control group using a device made with graphene ink. The poor responsivity of these control devices confirms that the synergistic effect of graphene and MOx is responsible for the high sensitivity of our sensors. Fig. 2c shows linear responsivity of the three ink formulations on logarithm of analyte concentration. The ZG-3 sample, corresponding to 3 wt% graphene loading, shows maximum enhancement (60% compared to that of pure ZnO) as interconnections between graphene sheets are optimized. We note that the ZG-3 sample also presents the best repeatability over testing cycles (Fig. 2d), whereas pure ZnO sample shows a distorted and declining response. This observation indicates that graphene stabilizes the gas detection performance in our sensing material formulation. However, significant baseline drifts along with slow recovery time reveal incomplete recovery to the initial state after a sensing event. We therefore attempt to establish an effective operation control algorithm to stabilize and optimize the sensing performance.

Optimization with temperature-pulsed modulation (TM) mode

Our proposed control mechanism implements modulation of temperature, exploiting the advantage of rapid heating and cooling cycle offered by the μHP platform. A key benefit of the pulses of heat, as opposed to constant heating, is that it helps to lower the power consumption, and extend the device lifetime. To understand the mechanisms of the TM mode, we first establish the physical representations of gas interactions at low and moderate temperature environments, as illustrated in Supplementary Fig. S7a, b, respectively. The sensing processes can be analyzed with surface adsorption, analyte diffusion, and carrier transport. We introduce the following relations to support the temperature-dependent sensing mechanisms we propose here. Surface adsorption involves an interplay between physisorption and chemisorption processes.[55] Physisorption typically occurs first and can be modeled by Lennard–Jones potential:

$$U(r,T) \propto \frac{\epsilon(T)}{n}\left(\frac{r_m(T)}{r}\right)^n \quad (1)$$

where U is potential energy, ϵ is depth of the potential well, r is the distance between the particles, and r_m is the distance at which the potential reaches its minimum. The relationship of physisorption with temperature is such that as temperature increases, the Lennard–Jones potential becomes more positive. The repulsive forces caused by the electron clouds of the adsorbate therefore dominate, resulting in less physisorption at high temperatures.[56,57] On the other hand, Chemisorption follows Arrhenius' law:[54]

$$k \propto \exp\left(\frac{-E_a}{R_g T}\right) \quad (2)$$

where k is chemical reaction rate, E_a is activation energy (≈0.5 eV

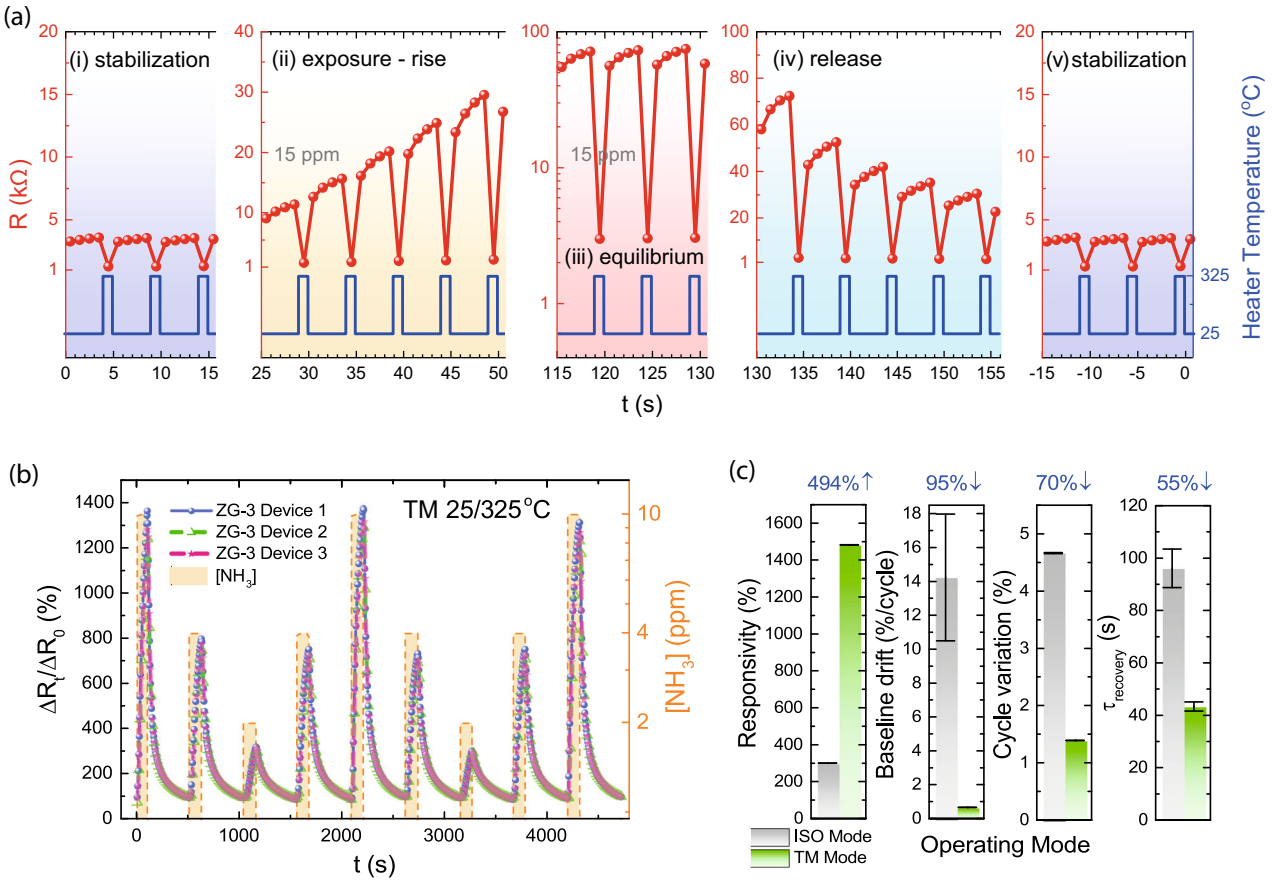

Fig. 3 Computation and performance of temperature modulation. **a** Stage-by-stage temporal response in TM mode. **b** Normalized response showing repeatability at various NH_3 concentrations, exhibited with three devices. **c** Performance enhancement of TM over ISO mode

for NH_3 on ZnO surface[58]), R_g is ideal gas constant (8.31 J mol^{-1} K^{-1}). Once the activation temperature is reached, a marginal increase in temperature leads to a dramatic increase in the reaction rate. Additionally, the resistivity for an electron to overcome a potential barrier can be associated with the following relationship:[54]

$$\rho \propto \exp\left(\frac{\Delta V}{k_B T}\right) \tag{3}$$

where ρ is the resistivity, ΔV is the change in potential barrier, k_B is the Boltzmann constant. Further, the diffusion rate and gas concentration diffused to the deepest layer of the active material can be described in the following equations based on Knudsen diffusion model.[20]

$$c(x = L) = c_{surf}\frac{m}{\cosh(m)}$$
$$m = L\left(\frac{k}{D_k}\right)^{1/2}, D_k \propto T^{1/2} \tag{4}$$

where D_k is diffusion rate, c_{surf} is analyte concentration at the surface and m is the proportion of analyte reaching distance L.

During low temperature (25 °C) period (Supplementary Fig. S7a), exothermic state for physisorption is maintained (Eq. (1)), while chemisorption is not activated (k in Eq. (2) is very low at 25 °C). Thus, physisorption of NH_3 at graphene sites and graphene/ZnO interfaces dominates chemisorption. From the bandgap perspective, fewer electrons are energized at low temperature (as inferred from Eq. (3)) to overcome the raised barrier arising from physisorption of NH_3 at the junctions, leading to a higher resistance. Additionally, gas diffusion is also promoted at this phase. D_k (in Eq. (4)) at 300 °C is 1.39 times than that at 25 °C, thus larger m at 25 °C indicates higher concentrations of NH_3 reaching the deepest layer at the room temperature. As the temperature increases, gas molecules tend to desorb from the surfaces, reducing the potential barrier ΔV, as illustrated in Supplementary Fig. S7b. At the same time, higher concentrations of electrons (Eq. (3)) are excited to pass through the lowered barrier. The dual effects of physisorption and electron transport further lower the electrical resistance as compared to that at low temperature. As the temperature increases above a threshold, the chemisorption activity (associated with adsorbed oxygen ion) is activated and the resistance starts to increase. From Eq. (2), k at 300 °C is 10^4 times than at 25 °C. To amplify responsivity, we thus select temperatures that maximize the electrical resistance difference based on Supplementary Fig. S5.

Next, we conduct a stage-by-stage temporal analysis which adapts the temperature dependency models we propose to develop a universal tool for the optimization process. The μHP is electrically pulsed to generate a train of heating pulses consisting of 325 °C pulse for 1 s (the μHP can reach 325 °C within 0.1 s) followed by 4 s of non-heating time. The time series responses from measurement data can be divided into four phases: stabilization, exposure-rise, equilibrium, and release; as presented in Fig. 3a. During the stabilization phase (Fig. 3a(i)), the resistance reaches a steady state corresponding to its temperature without exposure to the analyte gas. The decrease in resistance observed at the instant of the 325 °C temperature pulse corresponds to the enhancement of electron transport as depicted in Eq. (3). Note that the baseline slope, referring to the line connecting points at nominated 25 °C within each heating period, is attributed to cooling time for the devices. During the exposure phase (Fig. 3a (ii)), the devices are exposed to pure NH_3. Physisorption of NH_3

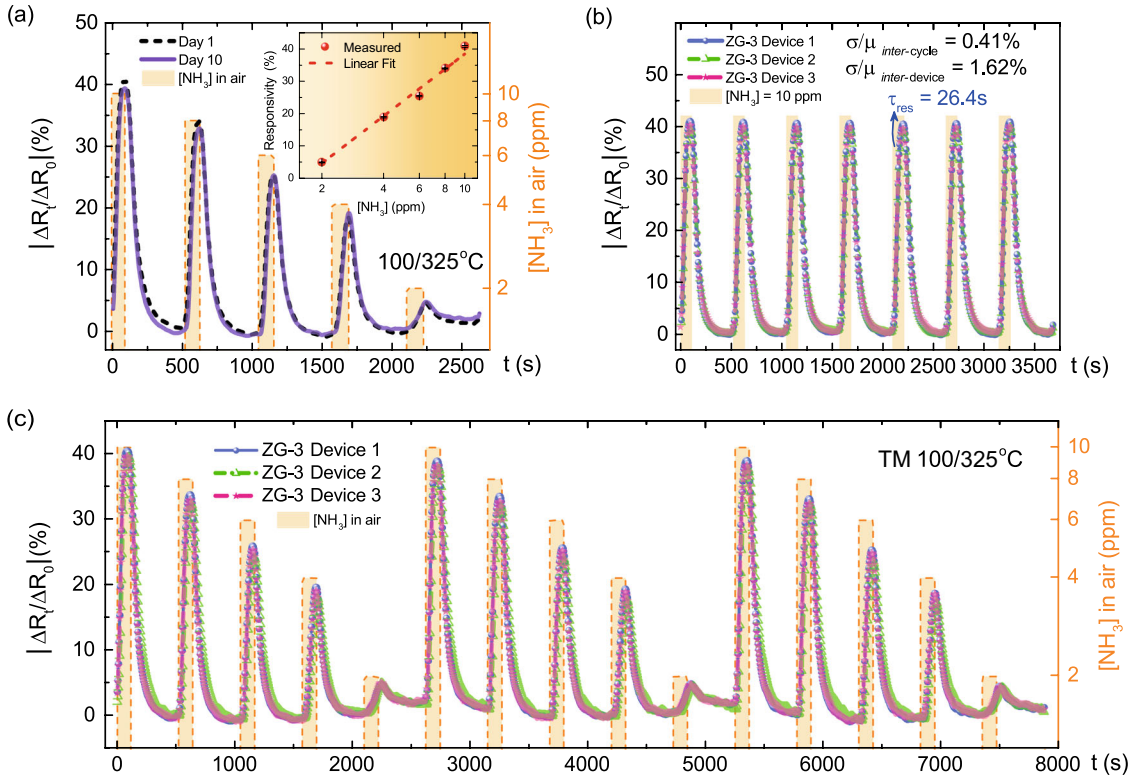

Fig. 4 Performance in air environment using TM mode. Plot using $|\Delta R_t/\Delta R_0|$ as *y*-axis. **a** Normalized response showing long-term stability over 10 days in air for five concentrations; (inset) responsivity as a function of concentration. **b** Normalized response showing repeatability (at 10 ppm) over seven cycles, exhibited with three devices. **c** Repeatability at step concentration over three cycles

molecules is promoted and dominates the adsorption process at 25 °C, building up potential barrier ΔV and thus ρ. While at 325 °C pulse, a sharp reduction in R is observed as the effect of T overrides that of increase in ΔV. The surface chemical reaction is also promoted at high temperature, but the response appears at the subsequent sampling point, as the carrier transport function responses faster than the chemisorption process.[55] After transiting back to low-temperature period, physisorption resumes dominating the process, accumulating more and more gas molecules in the sensing layer. Overall, the increasing trends shown by both the envelopes connecting $R_{25°C}$ and $R_{325°C}$, respectively, indicate molecule adsorption. Moreover, the slope of the envelope indicates the rate of adsorption corresponding to NH_3 concentration gradient which increases at first and then decreases until reaching equilibrium. Additionally, the baseline slope mentioned above also increases as NH_3 molecules are diffused to the deepest layer and are trapped at the later sampling points in each 25 °C period. When equilibrium (Fig. 3a(iii)) is reached during continuous flow of NH_3, the envelopes have a slope of ≈0, accounting for the equal rate of adsorption and desorption. During the release phase (Fig. 3a(iv)) in nitrogen (N_2) environment, desorption of NH_3 and byproducts are promoted by the pulses due to reduced physisorption and increased outward diffusion rate. The magnitude and slope of the envelope at low-temperature transient drop dramatically until reaching a steady state at 3 kΩ and ≈0, respectively (similar to Fig. 3a(i)), indicating gas adsorbed being fully desorbed.

The data processing steps to generate the device are detailed in Supplementary Notes and Supplementary Fig. S8a, b. The features are extracted based on the processed output curves (S_t). Inset of Supplementary Fig. S8b shows a linear relationship with respect to log of concentration. An average steady-state responsivity S of ≈1500% and sensitivity of 125%/ppm are achieved at 10 ppm with TM mode. Figure 3b shows a continuous S_t response consisting of nine cycles of NH_3 injection with decreasing and increasing concentration varying at steps of 10, 4, 2 ppm. The response curves of three devices measured simultaneously all demonstrate excellent repeatability and transient stability without apparent hysteretic behavior and baseline drift.

Figure 3c summarizes the comparison of performances between the TM and ISO modes. First, TM mode exhibits a responsivity improvement of 494% over ISO mode for ZG-3 at a same concentration which has a ΔR of 300%. Second, baseline drift is significantly reduced to 0.67% per cycle (95% improvement over ISO). Third, the repeatability of responsivity in TM mode shows 1.4% ± 0.08% of average cycle variation, representing an improvement of 70% over ISO mode. The improved repeatability and minimized drift can be attributed to the effectiveness of regeneration of the sensing layer due to the effective temperature modulation scheme. The average response and recovery time constants are also shortened, where τ_{res} drops from 45 s (ISO) to 28 s (TM), while τ_{rec} drops from 98 s (ISO) to 43 s (TM). The reduction in recovery time is attributed to the short pulses that accelerate the desorption of physisorbed gas molecules. Additionally, stabilization time is reduced from 60 min (ISO) to 5 min (TM), making the re-calibration process more practical. The device-to-device responsivity variation is within 0.5% (as shown in Fig. 3b), exhibiting good potential for mass production. The ultralow device-to-device performance variation is also attributed to the uniformity of inkjet deposition. We also note that the TM technique dramatically reduces power consumption without compromising response. The device consumes 6 mW at 25/325 °C, which is 78% more energy efficient than operation in ISO mode at optimal temperature of 300 °C and 92% more energy efficient than the state-of-art commercial MOS MEMS NH_3 sensor (MiCS-6814) that consumes

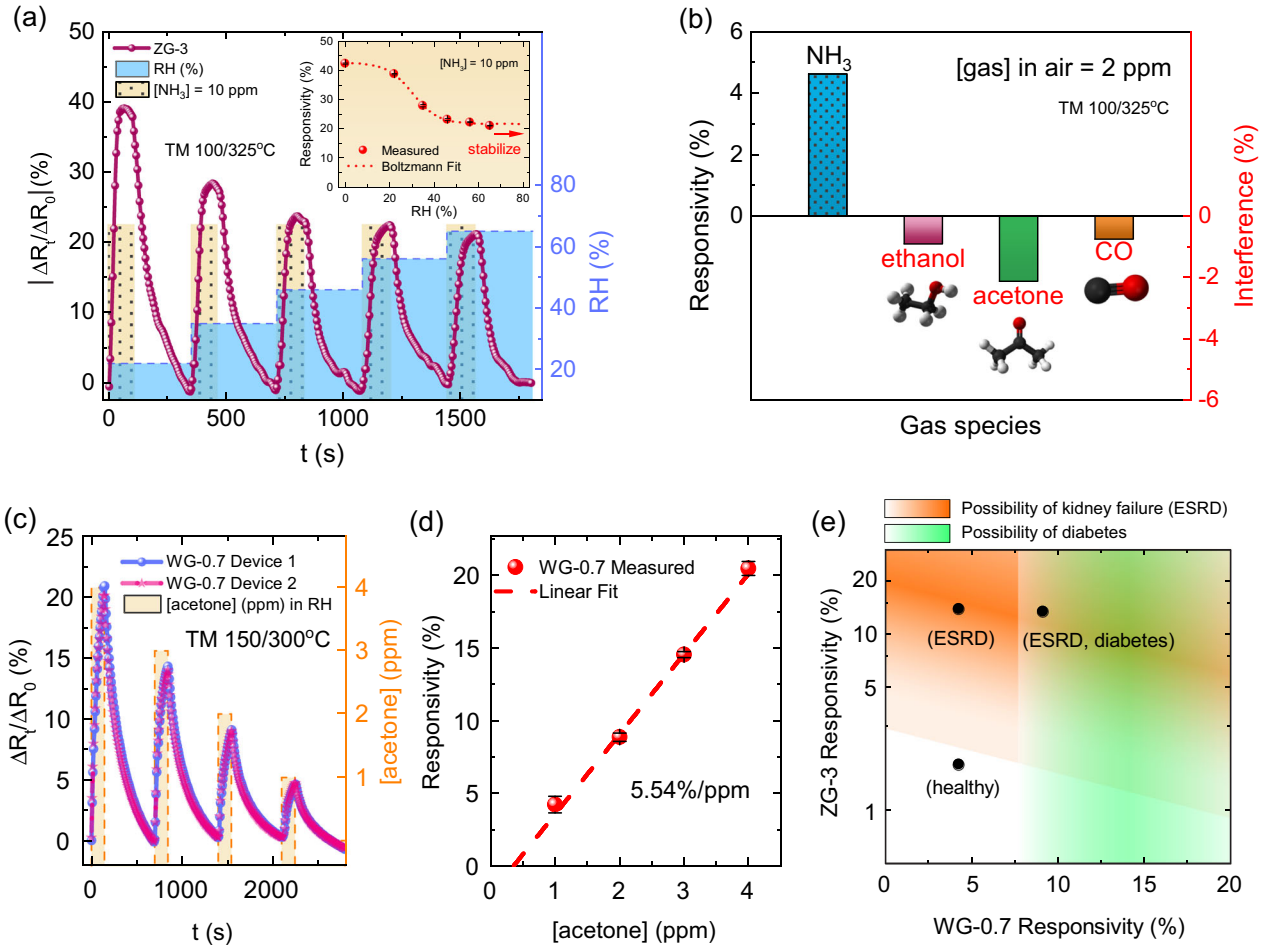

Fig. 5 Selectivity in TM mode. **a** Normalized response at 120/240 s NH_3 exposure/release cycles varied at various RH levels; (inset) responsivity as a function of RH levels. **b** Cross-analyte selectivity among common interfering gas species in exhaled breath. **c** Normalized response of two compensating WG-0.7 devices at 140/560 s acetone exposure/release cycles varied at 1–4 ppm. **d** WG-0.7 responsivity as a function of acetone concentration. **e** Mapping for tentative detection of kidney failure and diabetes using dual graphene–MOx sensors: ZG-3 and WG-0.7

73 mW. Moreover, the sensors demonstrate high SNR of >5600, with a calculated limit of detection down to 16 ppb (see Supplementary Notes for details).

Performance in the air environment

To proceed further towards the realization of breath analyzer, we next measure the device in synthetic air (SA) containing the major atmospheric composition, including nitrogen, oxygen, and carbon dioxide (CO_2). Introduction of SA results in O^- species being adsorbed onto the NP surfaces, transforming the detection of NH_3 into interactions with the adsorbed species.[52] Adsorption of NH_3 recedes the depletion region, leading to an increase in conductivity according to the concentration of NH_3.[52] We characterize the responsivity of NH_3 in the range of 2–10 ppm which falls into the primary interest of diagnosis of metabolic diseases. For instance, a mean of 4.88 ppm NH_3 may indicate that a patient has end-stage renal disease (ESRD),[59] i.e. kidney failure. We assume a detection threshold of 2 ppm NH_3, provided that 0.5–2 ppm of NH_3[60] are present in the breath of healthy adults. Fig. 4a shows the S_t response of NH_3 in SA varying at 2 ppm decreasing steps injected for 120 s for every 520 s period. The optimized temperature for the cooling period in TM mode is raised to 100 °C while the pulse temperature remains the same. The responsitivity (inset of Fig. 4a) extracted from the steady-state peaks of S_t at the concentration steps shows a linear relationship with logarithm of concentrations of NH_3, with a sensitivity of 4.2%/ppm. Moreover, the long-term stability study shows the well alignment between initial and measurements on 10th day with variations within 1%. The result in the performance reflects no sign of deterioration and drifts over the period under study. Furthermore, as shown in Fig. 4b, the variations of responsivity across injection cycles and across devices at 10 ppm are only 0.41% and 1.62%, respectively. Figure 4c further showcases the robustness of the sensors with continuous S_t consisting of 15 cycles of NH_3 injection with repeated decreasing concentration varying at 2 ppm steps. The response shows no notable hysteretic behavior (max hysteresis of ±0.34%), as reflected in Supplementary Fig. S9. τ_{res} is 26.4 s and the power consumption is 12.4 mW at the optimized TM scheme (100/325 °C) in SA environment. Despite increment of power, this still represents a 56% improvement over ISO mode.

Interference with other gases present in exhaled breath

The major components of breath of a healthy person contain 4% of CO_2,[61] 0–6 ppm of CO,[61] and <1 ppm of VOCs including acetone, isoprene, and ethanol.[62] However, MOx sensors often interfere with these analytes. To assess the influence of humidity on sensing performances, we characterize the response of NH_3 at 10 ppm in humidified SA at 22%, 35%, 45%, 56% and 65% RH levels, as shown in Fig. 5a. Water vapor introduces OH^- species that can be adsorbed on the surface of the sensing material, causing doping and reduction in the device responsivity. The

responsivity with respect to RH level (inset of Fig. 5a) is fitted with Boltzmann curve (Eq. (5)) as two plateaus within the ranges of RH < 20% and RH > 45% can be clearly distinguished.

$$S_{RH} = 21.62 + \frac{20.96}{1 + 0.1747\exp([RH] - 30.42)} \quad (5)$$

where S_{RH} is responsivity under RH. Although humidity reduces responsivity inevitability, a common phenomenon in chemiresistive sensors, our proposed TM operation allows interference to be mitigated and enables reliable characterization at high RH levels. We predict the responsivity at 80% RH (typical value in breath) to be 21.62% based on the fit from Eq. (5). The estimated value has only 0.04% variation from the measured value at 65% RH. One approach to reconstruct the accurate level of NH_3 in humid breath is to compensate the readings by 190% (value as if under dry air), and then refer to the relationships deduced from the inset of Fig. 4a. In addition, we note that within the TM mode as long as sufficient reaction time is attained, the measurements are invariant to analyte injection/release period. This can be seen from the shortened analyte release period to 240 from 400 s (from Fig. 4) without compromising the response curve. This demonstrates the algorithm's utility as a robust tool for performance optimization.

In addition to humidity, we assess the cross-analyte selectivity with ethanol, acetone, and carbon monoxide (CO) which are the common interfering gas species in exhaled breath. These species are measured at 2 ppm, which are above maximum levels a healthy human would exhale.[61,62] The cross-selectivity data in Fig. 5b indicates a relatively small amount of interference from ethanol and CO (0.91% and 0.75%, respectively) while the effect of acetone is more prominent (2.12%).

Compensation of cross-analyte interference with WO_3–graphene sensors for potential disease diagnostics

To compensate for the interference effects, we introduce a complementary acetone-selective graphene–MOx sensor. For this, we fabricate an inkjet-printed WO_3–graphene device, as shown in Supplementary Fig. S10. WO_3 is used as the MOx material for its superior selectivity towards acetone. This is due to its high electric dipole moment which promotes strong interaction with acetone[63] (dipole moment of 2.91 D) as compared to NH_3 (1.46 D), H_2O (1.85 D), and ethanol (1.69 D). The WO_3-0.7 wt% graphene (WG-0.7) devices we fabricate achieve stable and linear responses with 9.12% responsivity at 2 ppm of acetone (Fig. 5c), detection limit of 360 ppb, and sensitivity of 5.54%/ppm (Fig. 5d) when operated at TM 150–300 °C in RH above 65%. Well-alignment of device-to-device response is seen from Fig. 5c; whereas low cross-cycle variation is shown in Supplementary Fig. S11. Figure 5e maps tentative detection of kidney failure and diabetes (associated with acetone level[64]) based upon plausible readouts from dual graphene–MOx sensors, ZG-3 and WG-0.7, as if presented in the breath. The orange-shaded area indicates potential kidney failure with a probability distribution; the green-shaded area indicates potential diabetes; whereas the intersection indicates both diseases. The responsivity boundary from the breath of a healthy person measured by ZG-3 device, S_{ZG-3} (healthy), is estimated to be 1.82% (see Supplementary Notes). This readout is a result of combined contributions from 2 ppm NH_3 and 1 ppm VOC; whereas the readout point by WG-0.7, $S_{WG-0.7}$ (healthy), is 4.23%. The tilt angle of the orange-shaded boundary is determined by cross-correlation with the compensating WG-0.7 sensor. The typical responsivity from the breath of a patient with at least kidney failure (either with or without diabetes) measured by ZG-3 device, S_{ZG-3} (ESRD), is estimated to be 13.41–13.88% (see Supplementary Notes), which is contributed by 6 ppm NH_3 and acetone above 1 ppm. Note that patients with diabetes exhale 1.76–3.73 ppm of acetone.[64] The boundary for diabetes is thus determined at above 7.7% of WG-0.7 response.

DISCUSSION

Our sensor outperforms other nanomaterial-based counterparts in the literature (as shown in Supplementary Table 1) in almost every aspect, demonstrating the highest sensitivity, near-zero baseline drift, ultralow limit of detection, best SNR and stability, scalability, high device-to-device consistency, and ultralow power consumption. In addition, by harnessing the location-specific, uniform material deposition through our inkjet technology, a sensor array comprising a variety of graphene–MOx nanomaterials systems could be fabricated in a single multi-μHP CMOS die.[65] Coupling with common machine-learning techniques, such a multi-material system could offer further improved cross-analyte selectivity for multi-analyte breath diagnostics.

In summary, we have developed an inkjet-printed graphene–MOx-based sensor system that has been integrated onto miniaturized CMOS compatible platforms to selectively measure NH_3, a biomarker of kidney and liver problems, with fast and accurate performance. We have addressed the common issue of incomplete sensor regeneration faced by conventional MOx devices, through the establishment of temperature-dependent sensing mechanisms involving interplays between physisorption and chemisorption, diffusive mass transport, and electron transport processes via stage-by-stage temporal analysis. Through the development of effective temperature-modulation scheme, in pure NH_3, we achieve responsivity of 1500% at 10 ppm, sensitivity of 125%/ppm, significantly reduced baseline drift, τ_{res} of 28 s, τ_{rec} of 43 s, inter-device variation within 0.5%, SNR of 5600. In SA, we achieve long-term responsivity variations within 1%, inter-cycle variations within 0.41%, showing extraordinary repeatability and device-to-device consistency with no noticeable hysteretic behavior. Considering real-world scenarios, our sensors exhibit highly stabilized responses under high RH level. Furthermore, we deploy a parallel acetone-selective inkjet-printed WO_3–graphene sensor to compensate for the interference by acetone. Our strategy to combine the sensing material, inkjet printing onto CMOS MEMS platform and TM promises a robust system that outperforms conventional devices in aspects of reproducibility, performance reliability, recovery time while enhancing responsivity. The miniaturized platform and significant reduction in power consumption pave the way for the ubiquitous implementation of mobile-embedded devices for real-time wireless-connected personalized monitoring systems. The versatile technologies enable a multi-analyte sensor to be fabricated reliably and cost-effectively, offering new routes towards the development of multi-disease diagnostics platforms.

METHODS

Ink formulation

We ultrasonicate 100 mg of graphite (Sigma-Aldrich, 100 mesh flakes) with 1.5 mg PVP (Sigma-Aldrich, average molecular weight 10,000 Da) in mixture of 9 mL IPA and 1 mL 2-butanol for 12 h. The mixtures are sonicated for 12 h in a 20 kHz bath sonicator at 25 °C, centrifugated at 4030 rpm and the top 80% of resultant dispersion is collected. ZnO nanopowder (Sigma-Aldrich 677450) is dispersed in IPA, 2-butanol, PVP, and sonicated according to the above, and subsequently filtrated. Subsequently, the graphene and ZnO dispersions are mixed according to different graphene loading and sonicated for 30 min to produce the final ink which is then loaded into Fujifilm Dimatix DMP-2831 inkjet printer. The following parameters are set for the printer: drop spacing of 30 μm at 55 °C which forms continuous line morphology; inter-layer delay of 60 s.

Ink and film characterizations

UV-Vis: The dispersions are diluted to 10, 1, 1 vol% for graphene, ZnO/graphene, ZnO inks, respectively, to avoid detector saturation. Measured spectra of solvent with PVP are subtracted from the data. *Contact angle*: A 2 µL droplet is drop cast and measured via sessile drop technique at room temperature. *Rheology and surface tension*: The ink is characterized via pendant droplet and parallel plate rheometer measurements to determine the surface tension and the viscosity of the ink, respectively. Viscosity measurements are conducted at 5 °C to eliminate evaporation. *Raman*: The inkjet-printed graphene/ZnO layer onto CMOS device is used for the Raman measurement. An excitation wavelength of 514 nm and a duration of 10 s is used for each measurement point. *SEM*: Images of graphene/ZnO films are acquired with a high-resolution Magellan 400L SEM. The field emission gun is operated at 15 kV and 10 pA gun current. A 3 nm Au/Pd coating is sputtered onto the surface to reduce the build-up of electrons. *AFM*: The AFM samples are characterized with a Bruker Dimension Icon AFM in ScanAsyst^{TM} mode, using a silicon cantilever with a silicon nitride tip.

Gas characterization

Four CMOS devices are tested in the gas characterization rig simultaneously in an air-sealed stainless steel chamber, where the pressure is controlled at 1 atm. 2 ppm of NH_3 is produced from dilution of a NH_3 cylinder (BOC, 1000 ppm in Ar) by balancing 1 sccm of NH_3 and 500 sccm of N_2 or SA cylinder (BOC, zero grade air). The RH level of SA is controlled by balancing dry air with appropriate proportion of the humid air. The humid air is produced by passing dry air into water bubbler. Humidity sensor is used for RH characterization.

Electrical measurement

The devices are wire-bonded to DIP8 test package which fits in the pins that are solder-connected to external wires for a microprocesser board. Resistances of the sensors are evaluated by the voltage division of a series connection of pull-up resistance and sensor. $V_{supply} = 2.5$ V, $R_{pull-up}$ is selected to be comparable to R_{sensor} after the sensor is stabilized for ~5 min (TM mode). Multi-device readout is realized using a multiplexer followed by A/D converter to generate output to be transmitted using USB to PC interface for signal processing.

Signal processing

Processes involve filtering, envelope segmentation, normalization, feature extraction, and data analytics with PCA for dimensional reduction. LabView is used as the data acquisition interface. Matlab, Python, and Origin are used for signal processing, feature extraction, data classification, and data visualization.

DATA AVAILABILITY

All relevant data are available from the corresponding author on request.

Received: 2 April 2019; Accepted: 4 October 2019;
Published online: 05 November 2019

REFERENCES

1. Nakhleh, M. K. et al. Diagnosis and classification of 17 diseases from 1404 subjects via pattern analysis of exhaled molecules. *ACS Nano* **11**, 112–125 (2017).
2. Mathew, T., Pownraj, P., Abdulla, S. & Pullithadathil, B. Technologies for clinical diagnosis using expired human breath analysis. *Diagnostics* **5**, 27–60 (2015).
3. Spacek, L. A. et al. Repeated measures of blood and breath ammonia in response to control, moderate and high protein dose in healthy men. *Sci. Rep.* **8**, 2554 (2018).
4. Meng, Z., Stolz, R. M., Mendecki, L. & Mirica, K. A. Electrically-transduced chemical sensors based on two-dimensional nanomaterials. *Chem. Rev.* **119**, 478–598 (2019).
5. Chatterjee, B. & Bandyopadhyay, A. Development of zinc oxide sensors for detecting ammonia gas in the ambient air: a critical short review. *Environ. Qual. Manag.* **26**, 89–105 (2016).
6. Lin, Q., Li, Y. & Yang, M. Tin oxide/graphene composite fabricated via a hydrothermal method for gas sensors working at room temperature. *Sens. Actuators B* **173**, 139–147 (2015).
7. Wang, C. et al. Metal oxide gas sensors: sensitivity and influencing factors. *Sensors* **10**, 2088–2106 (2010).
8. Mao, S., Lu, G. & Chen, J. Nanocarbon-based gas sensors: progress and challenges. *J. Mater. Chem. A* **2**, 5573–5579 (2014).
9. Huang, Q., Zeng, D., Li, H. & Xie, C. Room temperature formaldehyde sensors with enhanced performance, fast response and recovery based on zinc oxide quantum dots/graphene nanocomposites. *Nanoscale* **4**, 5651 (2012).
10. Zhang, J., Liu, X., Neri, G. & Pinna, N. Nanostructured materials for room-temperature gas sensors. *Adv. Mater.* **28**, 795–831 (2016).
11. Singh, G. et al. ZnO decorated luminescent graphene as a potential gas sensor at room temperature. *Carbon* **50**, 385–394 (2012).
12. Tammanoon, N. et al. Ultrasensitive NO_2 Sensor Based on Ohmic Metal–semiconductor interfaces of electrolytically exfoliated graphene/flame-spray-made SnO_2 nanoparticles composite operating at low temperatures. *ACS Appl. Mater. Interfaces* **7**, 24338–24352 (2015).
13. Abideen, Z. U. et al. Excellent gas detection of ZnO nanofibers by loading with reduced graphene oxide nanosheets. *Sens. Actuators B* **221**, 1499–1507 (2015).
14. Tai, H. et al. ZnO nanoparticles/reduced graphene oxide bilayer thin films for improved NH_3-sensing performances at room temperature. *Nanoscale Res. Lett.* **11**, 130 (2016).
15. Renganathan, B., Sastikumar, D., Gobi, G., RajeswariYogamalar, N. & ChandraBose, A. Nanocrystalline ZnO coated fiber optic sensor for ammonia gas detection. *Opt. Laser Technol.* **43**, 1398–1404 (2011).
16. Shao, F. et al. NH_3 sensing with self-assembled ZnO-nanowire $_3$HP sensors in isothermal and temperature-pulsed mode. *Sens. Actuators, B* **226**, 110–117 (2016).
17. Liu, S., Yu, B., Zhang, H., Fei, T. & Zhang, T. Enhancing NO_2 gas sensing performances at room temperature based on reduced graphene oxide-ZnO nanoparticles hybrids. *Sens. Actuators B* **202**, 272–278 (2014).
18. Lu, G. et al. Toward practical gas sensing with highly reduced graphene oxide: a new signal processing method to circumvent run-to-run and device-to-device variations. *ACS Nano* **5**, 1154–1164 (2011).
19. Lin, Q., Li, Y. & Yang, M. Tin oxide/graphene composite fabricated via a hydrothermal method for gas sensors working at room temperature. *Sens. Actuators B* **173**, 139–147 (2012).
20. Suematsu, K. et al. Pulse-driven semiconductor gas sensors toward ppt level toluene detection. *Anal. Chem.* **90**, 11219–11223 (2018).
21. DeLuca, A. et al. Temperature-modulated graphene oxide resistive humidity sensor for indoor air quality monitoring. *Nanoscale* **8**, 4565–4572 (2016).
22. Rogers, P. H., Benkstein, K. D. & Semancik, S. Machine learning applied to chemical analysis: sensing multiple biomarkers in simulated breath using a temperature-pulsed electronic-nose. *Anal. Chem.* **84**, 9774–9781 (2012).
23. Hossein-Babaei, F. & Amini, A. A breakthrough in gas diagnosis with a temperature-modulated generic metal oxide gas sensor. *Sens. Actuators B* **166-167**, 419–425 (2012).
24. Lotya, M. et al. Liquid phase production of graphene by exfoliation of graphite in surfactant/water solutions. *J. Am. Chem. Soc.* **131**, 3611–3620 (2009).
25. Backes, C. et al. Guidelines for exfoliation, characterization and processing of layered materials produced by liquid exfoliation. *Chem. Mater.* **29**, 243–255 (2017).
26. Ng, L. W. T. et al. *Printing of Graphene and Related 2D Materials* 53–101 (Springer International Publishing, Cham, 2019).
27. Liang, Y. T. & Hersam, M. C. Highly concentrated graphene solutions via polymer enhanced solvent exfoliation and iterative solvent exchange. *J. Am. Chem. Soc.* **132**, 17661–17663 (2010).
28. Bourlinos, A. B. et al. Aqueous-phase exfoliation of graphite in the presence of polyvinylpyrrolidone for the production of water-soluble graphenes. *Solid State Commun.* **149**, 2172–2176 (2009).
29. Hasan, T. et al. Stabilization and âĂIJDebundlingâĂİ of single-wall carbon nanotube dispersions in N-methyl-2-pyrrolidone (NMP) by polyvinylpyrrolidone (PVP). *J. Phys. Chem. C* **111**, 12594–12602 (2007).
30. Dodoo-Arhin, D. et al. Inkjet-printed graphene electrodes for dye-sensitized solar cells. *Carbon* **105**, 33–41 (2016).
31. Faure, B. et al. Dispersion and surface functionalization of oxide nanoparticles for transparent photocatalytic and UV-protecting coatings and sunscreens. *Sci. Technol. Adv. Mater.* **14**, 023001 (2013).
32. Guo, L. et al. Highly monodisperse polymer-capped ZnO nanoparticles: preparation and optical properties. *Appl. Phys. Lett.* **76**, 2901 (2000).
33. Arapov, K. et al. Conductive screen printing inks by gelation of graphene dispersions. *Adv. Funct. Mater.* **26**, 586–593 (2016).
34. Bolten, D. & Turk, M. Experimental study on the surface tension, density, and viscosity of aqueous poly(vinylpyrrolidone) solutions. *J. Chem. Eng. Data* **56**, 582–588 (2011).
35. Torrisi, F. et al. Inkjet-printed graphene electronics. *ACS Nano* **6**, 2992–3006 (2012).

36. Deegan, R. D. et al. Capillary flow as the cause of ring stains from dried liquid drops. *Nature* **389**, 827–829 (1997).
37. Deegan, R. D. et al. Contact line deposits in an evaporating drop. *Phys. Rev. E* **62**, 756–765 (2000).
38. Hu, G. et al. Black phosphorus ink formulation for inkjet printing of optoelectronics and photonics. *Nat. Commun.* **8**, 278 (2017).
39. Hu, G. et al. Functional inks and printing of two-dimensional materials. *Chem. Soc. Rev.* **47**, 3265–3300 (2018).
40. Luo, S., Harris, T. & Wong, C. Study on surface tension and adhesion for flip chip packaging. In *Proc. International Symposium on Advanced Packaging Materials Processes, Properties and Interfaces*, 299–304 (2001).
41. Derby, B. Inkjet printing of functional and structural materials: fluid property requirements, feature stability, and resolution. *Annu. Rev. Mater. Res.* **40**, 395–414 (2010).
42. Ali, S., Udrea, F., Milne, W. & Gardner, J. Tungsten-based SOI microhotplates for smart gas sensors. *J. Microelectromech. Syst.* **17**, 1408–1417 (2008).
43. Secor, E. B., Prabhumirashi, P. L., Puntambekar, K., Geier, M. L. & Hersam, M. C. Inkjet printing of high conductivity, flexible graphene patterns. *J. Phys. Chem. Lett.* **4**, 1347–1351 (2013).
44. Al-Hada, N. M. et al. A facile thermal-treatment route to synthesize ZnO nanosheets and effect of calcination temperature. *PLoS One* **9**, e103134 (2014).
45. Jussila, H. et al. New approach for thickness determination of solution-deposited graphene thin films. *ACS Omega* **2**, 2630–2638 (2017).
46. Zinc oxide. https://www.sigmaaldrich.com/catalog/product/aldrich/677450. Accessed Oct 2019.
47. Wu, J.-B., Lin, M.-L., Cong, X., Liu, H.-N. & Tan, P.-H. Raman spectroscopy of graphene-based materials and its applications in related devices. *Chem. Soc. Rev.* **47**, 1822–1873 (2018).
48. Ferrari, A. C. & Basko, D. M. Raman spectroscopy as a versatile tool for studying the properties of graphene. *Nat. Nanotechnol.* **8**, 235–246 (2013).
49. Chen, S. J. et al. Structural and optical properties of uniform ZnO nanosheets. *Adv. Mater.* **17**, 586–590 (2005).
50. Cançado, L. G. et al. Quantifying defects in graphene via raman spectroscopy at different excitation energies. *Nano Lett.* **11**, 3190–3196 (2011).
51. Santra, S. et al. CMOS integration of inkjet-printed graphene for humidity sensing. *Sci. Rep.* **5**, 17374 (2015).
52. Lupan, O. et al. Sensing performances of pure and hybridized carbon nanotubes-ZnO nanowire networks: a detailed study. *Sci. Rep.* **7**, 14715 (2017).
53. Guan, Z., Ni, S. & Hu, S. Band gap opening of graphene by forming a graphene/$PtSe_2$ van der Waals heterojunction. *RSC Adv.* **7**, 45393–45399 (2017).
54. Das, S. & Jayaraman, V. SnO_2: a comprehensive review on structures and gas sensors. *Prog. Mater. Sci.* **66**, 112–255 (2014).
55. Bai, J. & Zhou, B. Titanium dioxide nanomaterials for sensor applications. *Chem. Rev.* **114**, 10131–10176 (2014).
56. Nasehzadeh, A., Mohseni, M., Azizi, K. & Azizi, K. The effect of temperature on the Lennard–Jones (6-12) pair potential function. *J. Mol. Struct. THEOCHEM* **589-590**, 329–335 (2002).
57. Damyanova, M., Balabanova, E. & Hohm, U. Temperature-dependent interaction potential between NF_3 molecules and thermophysical properties of gaseous NF_3. *J. Phys. Conf. Ser.* **514**, 012055 (2014).
58. Nancy Anna Anasthasiya, A., Rai, P. & Jeyaprakash, B. Understanding ammonia adsorption and charge transfer process on ZnO using experimental and DFT approach. *Mater. Chem. Phys.* **214**, 540–547 (2018).
59. Li, H.-Y., Lee, C.-S., Kim, D. H. & Lee, J.-H. Flexible room-temperature NH_3 sensor for ultrasensitive, selective, and humidity-independent gas detection. *ACS Appl. Mater. Interfaces* **10**, 27858–27867 (2018).
60. Schmidt, F. M. et al. Ammonia in breath and emitted from skin. *J. Breath Res.* **7**, 017109 (2013).
61. Hibbard, T. & Killard, A. J. Breath ammonia analysis: clinical application and measurement. *Crit. Rev. Anal. Chem.* **41**, 21–35 (2011).
62. Lindinger, W. & Jordan, A. Proton-transfer-reaction mass spectrometry (PTR-MS): on-line monitoring of volatile organic compounds at pptv levels. *Chem. Soc. Rev.* **27**, 347 (1998).
63. Righettoni, M., Tricoli, A. & Pratsinis, S. E. Si:WO_3 sensors for highly selective detection of acetone for easy diagnosis of diabetes by breath analysis. *Anal. Chem.* **82**, 3581–3587 (2010).
64. Deng, C., Zhang, J., Yu, X., Zhang, W. & Zhang, X. Determination of acetone in human breath by gas chromatography-mass spectrometry and solid-phase microextraction with on-fiber derivatization. *J. Chromatogr. B* **810**, 269–275 (2004).
65. Udrea, F., Ali, S. & Gardner, J. CMOS micro-hotplate array design for nanomaterial-based gas sensors. In *Proc. 2008 International Semiconductor Conference*, 143–146 (2008).

ACKNOWLEDGEMENTS

We acknowledge support from Alphasense Limited and EPSRC (EP/L016087/1).

AUTHOR CONTRIBUTIONS

T.-C.W. designed and conducted the experiments, developed the control algorithms, and analyzed the data. X.Z., T.A.-O. performed SEM and Raman characterizations. T.H. supervised the project. T.-C.W., T.H. prepared the manuscript. All authors analyzed and discussed the results and contributed to the final manuscript.

COMPETING INTERESTS

The authors declare no competing interests.

ADDITIONAL INFORMATION

Supplementary information is available for this paper at https://doi.org/10.1038/s41699-019-0125-3.

Correspondence and requests for materials should be addressed to T.H.

Reprints and permission information is available at http://www.nature.com/reprints

Publisher's note Springer Nature remains neutral with regard to jurisdictional claims in published maps and institutional affiliations.